New insights on intraplate volcanism in French Polynesia from wavelet analysis of GRACE, CHAMP, and sea surface data

I Panet, Aude Chambodut, M Diament, M Holschneider, O Jamet

New insights on intraplate volcanism in French Polynesia from wavelet analysis of GRACE, CHAMP, and sea surface data

I. Panet,[1,2] A. Chambodut,[3] M. Diament,[1] M. Holschneider,[3] and O. Jamet[2]

Received 3 November 2005; revised 21 April 2006; accepted 5 May 2006; published 23 September 2006.

[1] In this paper, we discuss the origin of superswell volcanism on the basis of representation and analysis of recent gravity and magnetic satellite data with wavelets in spherical geometry. We computed a refined gravity field in the south central Pacific based on the GRACE satellite GGM02S global gravity field and the KMS02 altimetric grid, and a magnetic anomaly field based on CHAMP data. The magnetic anomalies are marked by the magnetic lineation of the seafloor spreading and by a strong anomaly in the Tuamotu region, which we interpret as evidence for crustal thickening. We interpret our gravity field through a continuous wavelet analysis that allows to get a first idea of the internal density distribution. We also compute the continuous wavelet analysis of the bathymetric contribution to discriminate between deep and superficial sources. According to the gravity signature of the different chains as revealed by our analysis, various processes are at the origin of the volcanism in French Polynesia. As evidence, we show a large-scale anomaly over the Society Islands that we interpret as the gravity signature of a deeply anchored mantle plume. The gravity signature of the Cook-Austral chain indicates a complex origin which may involve deep processes. Finally, we discuss the particular location of the Marquesas chain as suggesting that the origin of the volcanism may interfere with secondary convection rolls or may be controlled by lithospheric weakness due to the regional stress field, or else related to the presence of the nearby Tuamotu plateau.

Citation: Panet, I., A. Chambodut, M. Diament, M. Holschneider, and O. Jamet (2006), New insights on intraplate volcanism in French Polynesia from wavelet analysis of GRACE, CHAMP, and sea surface data, *J. Geophys. Res.*, *111*, B09403, doi:10.1029/2005JB004141.

1. Introduction

[2] Intraplate volcanism in the south central Pacific has been attracting curiosity and interest among geoscientists for many years. Indeed, it shows many geophysical and geochemical features suggesting that active processes occur in the underlying mantle. For example, the seafloor is anomalously shallow, leading *McNutt and Fischer* [1987] to name it "superswell." Seismic velocities are too slow in the area [*McNutt and Judge*, 1990; *Ekström and Dziewonski*, 1998], and the geoid is marked by a negative anomaly. This indicates the presence of a broad convective upwelling in the mantle underlying French Polynesia, associated with a low-viscosity zone in the upper mantle [*McNutt and Judge*, 1990]. This upwelling interacts with the oceanic lithosphere to produce 14% of the Earth's volcanism in less than 5% of its surface [*Sleep*, 1990; *McNutt*, 1998]. Thus the area is marked by many volcanic chains, represented on Figure 1.

[3] A large part of the Polynesian volcanism is, however, difficult to explain in the frame of the classical plume theory. This theory assumes that hot spot tracks are formed consequently to the drift of tectonic plates over narrow, stationary mantle upwellings named plumes, anchored at depth [*Morgan*, 1972]. However, such a model does not account, for instance, for the radiometric ages obtained for many Polynesian islands, that do not follow the linear age progression along the chain expected in the case of a stationary plume [see, e.g., *Turner and Jarrard*, 1982]. Other models have also been proposed to explain intraplate volcanism, such as superficial upwellings [*Richter*, 1973; *Anderson*, 1995, 1998] or oscillating domes [*Davaille*, 1999]. The different approaches have been summarized by *Courtillot et al.* [2003]. However, none of these models could provide a thorough explanation of the volcanism occurring in this area. Among all geophysical observables, gravity and magnetism can help to comprehend the geodynamical processes involved. Our aim is thus to bring new insights on the processes at stake in French Polynesia, and in particular on the depth at which the volcanism finds its origin, by analyzing new gravity and magnetic data.

[1] Institut de Physique du Globe de Paris, Paris, France.
[2] Laboratoire de Recherche en Géodésie, Institut Géographique National, Marne-la-Vallée, France.
[3] Department of Applied and Industrial Mathematics, University of Potsdam, Potsdam, Germany.

0148-0227/06/2005JB004141$09.00

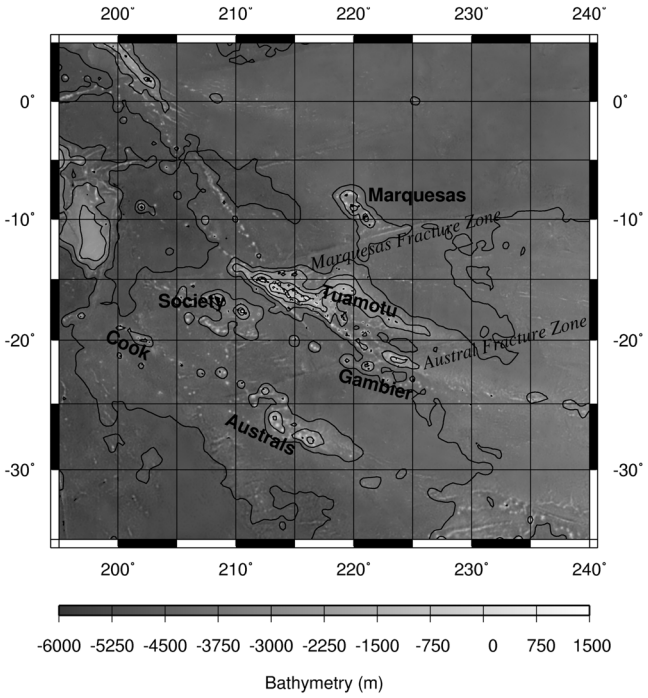

Figure 1. Bathymetric map of French Polynesia, based on the bathymetric grid by *Smith and Sandwell* [1997] version 8.2.

[4] At large wavelengths, the gravity field (geoid or gravity anomalies) can be used to constrain the viscosity structure of the Earth's mantle [*Hager et al.*, 1985]. At smaller wavelengths, it gives an insight into lithospheric structure. Jointly analyzed with bathymetric data, it allows to determine the compensation mechanisms of the seafloor topography [*Vening-Meinesz*, 1941; *Walcott*, 1970; *Watts*, 1978]. With the launch of satellite missions CHAMP (2000) and GRACE (2002), highly precise data are available at a resolution larger than 200 km. They lead to a valuable improvement of our knowledge of the gravity field over oceans when combined with higher resolution data such as altimetry.

[5] At large wavelengths, the internal magnetic field of the Earth is mainly dipolar and dominated by the core field [*Lowes*, 1974]. At smaller wavelengths, it is produced by spatial variations in the magnetization of crustal rocks. Thus the crustal magnetic field may directly be related to seafloor spreading lineations and geological structures. Thanks to the satellite data provided by Magsat (1979), Ørsted (1999), CHAMP (2000), and SAC-C (2000) missions, new representations of the crustal field become available with a resolution reaching 450 km [*Sabaka et al.*, 2004; *Maus et al.*, 2006].

[6] Our aim in this paper is to discuss the origin of intraplate volcanism in the south central Pacific. For that purpose, we first carry out a wavelet representation of gravity and magnetic data provided by the last generation of satellites. Then we develop a new method for analyzing the resulting anomalies, also using wavelets. Wavelets are specifically suited to study this area, which is characterized by a superimposition of structures on a broad range of scales. Thus multiscale techniques are a valuable tool to isolate and image the different contributions, from the lithospheric ones to the deeper ones.

2. Representation of Potential Fields: Discrete Wavelet Transform

2.1. Why Use Discrete Wavelets?

[7] To derive new representations of the gravity and magnetic fields, we chose to use spherical Poisson wavelets for the following reasons. First, such wavelets are functions which are defined not only on the sphere, but also in the whole space outside the sphere. Indeed, they admit a harmonic continuation outside the sphere and thus satisfy the Laplace equation [*Holschneider et al.*, 2003]. For that reason, we represent the gravity and the magnetic potentials as a superposition of such wavelets. Other quantities directly derived from the potential, such as the geoid, gravity anomalies or the magnetic field can be directly deduced from the wavelet representation of the potential.

[8] Second, it is possible to combine measurements at different altitudes within the wavelet representation because the wavelets are defined outside the sphere. This is a major asset since it allows to merge heterogeneous data sets. In addition, the wavelet representation can take into account the varying spectral characteristics of data of different origins. Low- (high-) resolution data may be efficiently represented by large (small) scale wavelets.

[9] Finally, contrary to the widely used spherical harmonics, the wavelets are well localized in space domain. Linear combinations of spherical harmonics can also be used to achieve spatial localization [see, e.g., *Wieczorek and Simons*, 2005; *Lesur*, 2006; *Simons et al.*, 2006], but the spherical Poisson wavelets that we use allow more direct computations [*Holschneider et al.*, 2003]. Thus we may build a local wavelet representation by only considering wavelets in a neighborhood of the area of interest. The number of wavelets necessary for local representations is then much smaller than the number of spherical harmonics, allowing easier computations of high-resolution representations. However, there is a trade-off between the scale starting from which such a local representation coincides with the restriction of a global model and the size of the region. This is due to the very nature of potential fields as solutions of Laplace equation. No perfect localization is possible.

2.2. How to Compute a Wavelet Representation?

[10] We choose to use the Poisson multipole wavelets that are well suited for potential fields representation. A thorough description of the wavelets is given by *Holschneider et al.* [2003]. We use Poisson multipole wavelets of order 3 for gravity representations and of order 2 for magnetic representations, as explained by *Chambodut et al.* [2005]. Figure 2 shows a cross section of Poisson multipole wavelets of order 3.

[11] We implement a wavelet family according to *Chambodut et al.* [2005]. All the wavelets are translated copies of a one-parameter family of mother wavelets at different scales. Since no natural dilation operator exists on the sphere, the different scales have to be constructed "by hand." At small scales, however, the wavelets behave like dilated copies of a single mother wavelet (I. Iglewska-Nowak and M. Holschneider, manuscript in preparation, 2006). We choose a discrete sequence of scales in order to

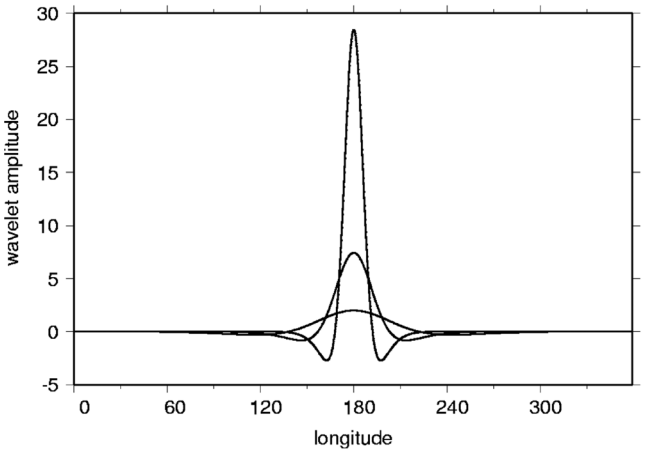

Figure 2. Cross section of Poisson multipole wavelets of order 3 and scales 1.5, 0.75, and 0.375 centered at point (0°, 0°).

fully cover the data spectra. The scales used for gravity and magnetic representations are given in Tables 1 and 2. A wavelet at a given scale is then shifted to a set of positions to fully cover the surface of the sphere. In order to get a complete representation, the number of positions at a given scale increases when the scale of the wavelet decreases. The collection of such functions forms a frame.

[12] To compute the wavelet representation, we apply a least squares adjustment of the data as explained by *Holschneider et al.* [2003] and *Chambodut et al.* [2005]. We add regularization to ensure the smoothness of the resulting gravity and magnetic potentials. This allows to choose a unique set of wavelet coefficients that both leads to a good fit of the data and a global smoothness of the potential. On the basis of our a priori knowledge of the smoothness of the gravity and magnetic potentials, the regularization matrix describes how the energy decreases from the large scales to the small ones. Its computation is detailed in the abovementioned references. The balance between the regularization and the fit of the data is then chosen in order to avoid the wavelet representation to fit the data with a precision higher than their noise, and to avoid a too smooth solution.

2.3. Gravity Field

2.3.1. Data

[13] The wavelet representation of the gravity field is adjusted on two different types of data: (1) free-air gravity anomalies derived from the global spherical harmonics representation GGM02S [*Tapley et al.*, 2004] up to degree and order 100 (it is based on 363 days of GRACE mission measurements between April 2002 and December 2003; the precision on the geoid is about 2–3 mm at 400 km resolution, the geoid varying between −100 m and +80 m) and (2) free-air gravity anomalies from the KMS 2002 satellite-altimetry-derived grid [*Andersen and Knudsen*, 1998]. The resolution of this grid is a few kilometers.

[14] These two kinds of data are complementary. Indeed, the GRACE-derived GGM02S gravity field is extremely precise at large wavelengths, whereas the gravity anomalies computed from satellite altimetry bring the high-resolution information. We also considered the use of ship data to improve the gravity field representation. The ship tracks we considered come from the compilation by *Adam and Bonneville* [2005]. We carried out comparisons between altimetric data and ship data along the ship tracks, and concluded that at wavelengths larger than about 10 kilometers, ship data are in good agreement with altimetric data. Ship data prove their utility when dealing with the smallest wavelengths of the gravity field or coastal areas, where the quality of altimetric data degrades. However, the available cruises with precise GPS positioning are very sparse around the Marquesas (where we compute our high-resolution gravity field). Consequently, ship data do not really improve our gravity field and we choose not to include them in our calculations.

2.3.2. Deriving the Wavelet Representation

[15] The gravity potential anomaly T is written as an infinite superposition of wavelets:

$$T = \sum_{i=1}^{\infty} \alpha_i \psi_i, \tag{1}$$

where ψ_i is the wavelet number i. However, for practical applications we have to approximate this infinite summation with a finite one, as stressed by *Holschneider et al.* [2003]. For GGM02S data, the observation equations are the same as those of *Chambodut et al.* [2005]. We actually compute gravity disturbances from GGM02S spherical harmonics expansion of the gravity potential.

[16] For KMS data, the observation equations are given by

$$\Delta g_{\mathrm{KMS}} - \epsilon_P - \epsilon_H - \epsilon_\gamma = -\sum_i \alpha_i \left(\frac{\partial \psi_i}{\partial r} + \frac{2\psi_i}{r} \right), \tag{2}$$

Table 1. Sequence of Scales Chosen for the Wavelets Used in Gravity Field Representation

Level	Scale (Nondimensionalized)	Scale, km
1	1.5	4955
2	0.75	3365
3	0.375	1995
4	0.1875	1090
5	0.09375	570
6	0.046875	290
7	0.023438	150
8	0.011719	75
9	0.005859	37
10	0.0029297	20

Table 2. Sequence of Scales Chosen for the Wavelets Used in Crustal Magnetic Anomaly Field Representation

Level	Scale (Nondimensionalized)	Scale,[a] km
1	2	5911
2	1	4426
3	0.5	2904
4	0.25	1808
5	0.125	1145
6	0.0625	786
7	0.03125	596

[a]At the mean altitude of 400 km.

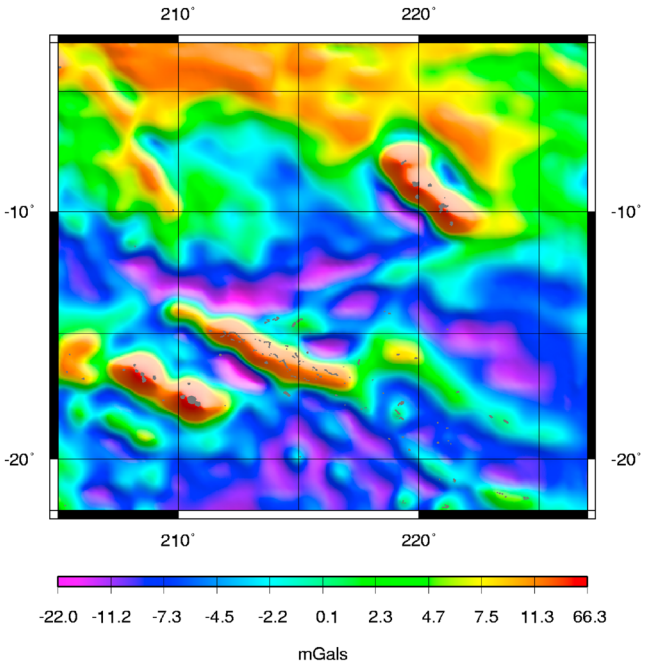

Figure 3. Gravity anomalies computed from the wavelet representation combining gravity anomalies from GGM02S global gravity field and KMS 2002 altimetric grid. Resolution about 75 km; 9692 wavelets are used.

where Δg_{KMS} is the gravity anomaly in the geodetic sense, defined as the difference between the intensity of the real gravity field at the measurement point and the intensity of the normal gravity field at the corresponding point on the telluroid [*Moritz*, 1989; *Hackney and Featherstone*, 2003]. In the spherical approximation, it is related to the gravity potential anomaly T by $\Delta g = -(\partial T/\partial r) - 2(T/r)$. For a higher accuracy, perturbation terms ϵ_P, ϵ_H, and ϵ_γ are added. The term ϵ_P accounts for the difference between the gravity anomaly and the isozenithal projection of the gravity anomaly vector that should in theory be inserted in the fundamental boundary condition; ϵ_H and ϵ_γ account for the effect of the Earth's ellipticity up to the order of the eccentricity squared. Detailed expressions of these perturbation terms are given by *Pavlis* [1988]. However, the total amplitude of the perturbation terms ϵ_P, ϵ_H, and ϵ_γ is smaller than 0.1 mGal in the studied area. We thus neglect them.

[17] We apply an iterative procedure to progressively compute the wavelet coefficients from the largest scales to the smallest ones. This allows to properly constrain the wavelet coefficients at all scales while keeping the size of the systems to solve under control. We progressively compute the wavelet coefficients from successive least squares fits of data of increasing resolution and decreasing spatial support, truncating the wavelet sum of equation (1) at smaller and smaller scales at each iteration. At each step, we only readjust the smallest scale of the previous iteration, the larger scales being fixed. Indeed, correlations between wavelets are small for consecutive scales, and negligible for nonconsecutive scales.

[18] We first compute the large-scale wavelet coefficients by a least squares adjustment of a global data set at low resolution from GGM02S gravity field. We then compute a wavelet representation down to 150 km resolution combining gravity data from GGM02S and from KMS 02 altimetric grid. It is based on 4981 wavelets with scales ranging between 4955 and 74 km. We jointly adjust 1836 gravity anomalies from GGM02S model up to degree and order 100, and 1755 gravity anomalies from KMS 2002 grid filtered at a 150 km resolution. To control the resolution of KMS 2002 free-air anomalies, we apply Jekeli's Gaussian filter of 150 km radius [*Jekeli*, 1981]. Residuals with respect to gravity anomalies derived from GGM02S and KMS gravity anomalies do not exceed 0.5 mGal in general, showing that KMS altimetric grid is consistent with space gravity data at this level of precision.

[19] We further increase the resolution of the wavelet representation down to 75 km by adding smaller scales determined by adjustment of 5641 data including 3886 gravity anomalies from KMS grid at 75 km resolution, and 1755 gravity anomalies from GGM02S gravity field filtered as previously. The smallest wavelet scale is 37 km. The resulting wavelet representation is composed of 9692 wavelets (Figure 3). Residuals with respect to gravity anomalies derived from GGM02S gravity field (Figure 4)

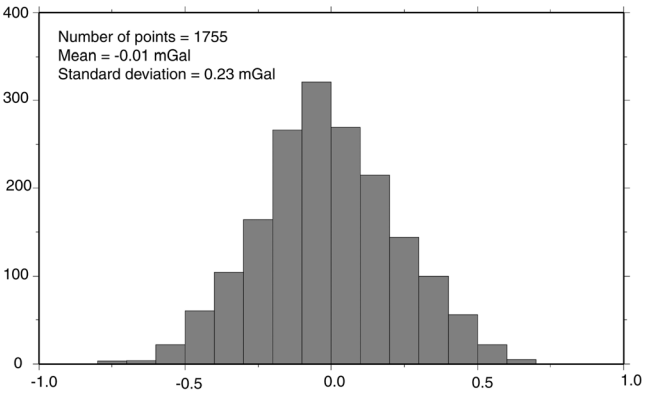

Figure 4. Histogram of residuals on the gravity anomaly (initial data from GGM02S global gravity field minus approximated data from 9692 wavelet representation) at 75 km resolution.

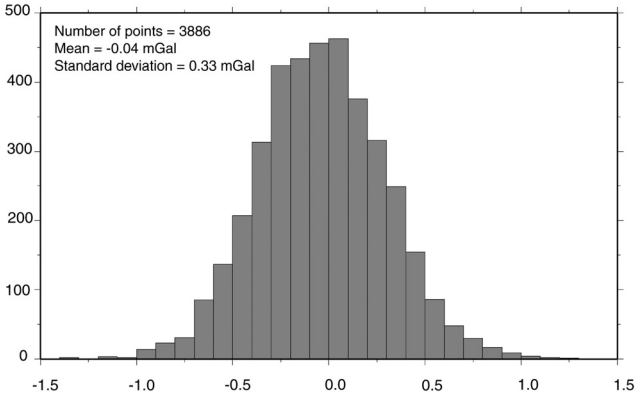

Figure 5. Histogram of residuals on the gravity anomaly (initial data from KMS 2002 satellite-derived gravity anomalies minus approximated data from 9692 wavelet representation) at 75 km resolution.

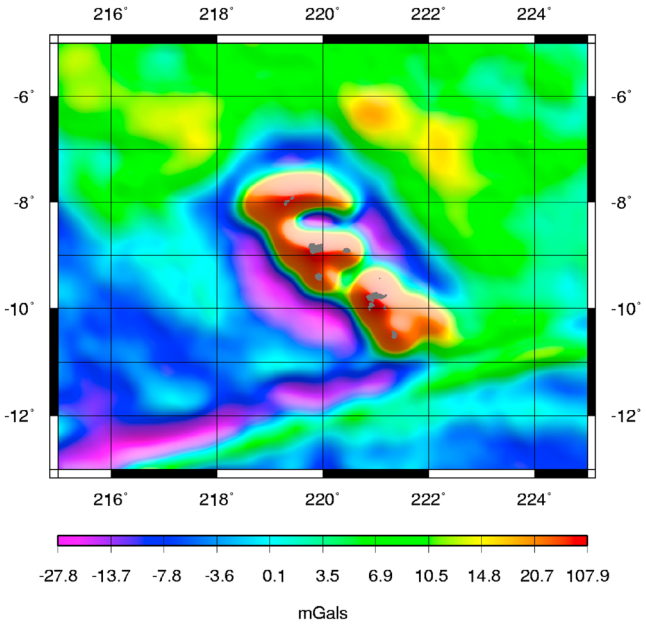

Figure 6. Gravity anomalies computed from the wavelet representation combining gravity anomalies from GGM02S global gravity field and KMS 2002 altimetric grid. Resolution about 35 km; 9651 wavelets are used.

and KMS gravity anomalies (Figure 5) are smaller than 0.5 mGal.

[20] The regional gravity field now having been computed, we finally perform a zoom on the Marquesas Islands. To that aim, we adjust 8000 free-air gravity anomalies data from KMS 02 altimetric grid at about 35 km resolution and add wavelets at scale 20 km. The resulting gravity field (composed of 9651 wavelets) is represented in Figure 6. Residuals with respect to KMS gravity anomalies (Figure 7) are mainly smaller than 1 mGal. However, we notice larger residuals near the coastlines, where the spatial variability of the gravity field is the highest, as shown on Figure 8. Those larger residuals may reflect the fact that the wavelet representation is slightly too smooth and that wavelets at smaller scales should be added near the islands.

2.3.3. Results

[21] Our approach allowed us to compute a local representation of the gravity field combining different data sets. Instead of about 300,000 spherical harmonics, only 9651 wavelets were necessary to represent the gravity field at 35 km resolution. This underlines the interest of wavelets for local gravity field computation.

[22] Because the gravity field in French Polynesia is the result of many processes that occur over a wide range of spatial scales, it displays anomalies at different spatial scales. To bring new insights in the origin of intraplate volcanism, it is necessary to analyze it at different resolutions and this will be the subject of section 3.

2.4. Magnetic Field

2.4.1. Data

[23] To represent the crustal magnetic field, we use the data provided by the low-orbit CHAMP satellite over the period 2000–2004. These data are corrected from various contributions associated to terrestrial and solar magnetic dynamos (see http://www.gfz-potsdam.de/pb2/pb23/SatMag/litmod4.html). Those corrections are detailed by *Maus et al.* [2006]. First, an internal field to degree/order 15, an external field to degree/order 2 and a predicted field due to eight main ocean tidal flows, are subtracted from the data. The tidal flow correction corresponds to the effect of conducting seawater flow through the Earth's magnetic field, which induces currents and gives rise to secondary magnetic fields clearly identified in magnetic satellite data [*Tyler et al.*, 2003; *Kuvshinov and Olsen*, 2005]. Second, the contributions produced by the polar electrojet around ±70° geomagnetic latitude are removed through a track-by-track algorithm.

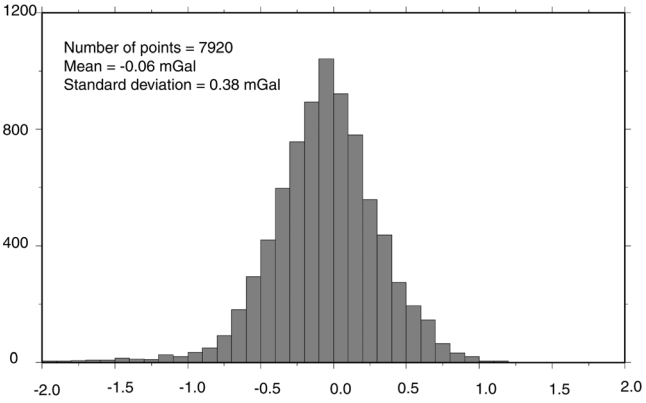

Figure 7. Histogram of residuals on the gravity anomaly (initial data from KMS 2002 satellite-derived gravity anomalies minus approximated data from 9651 wavelet representation) at 35 km resolution.

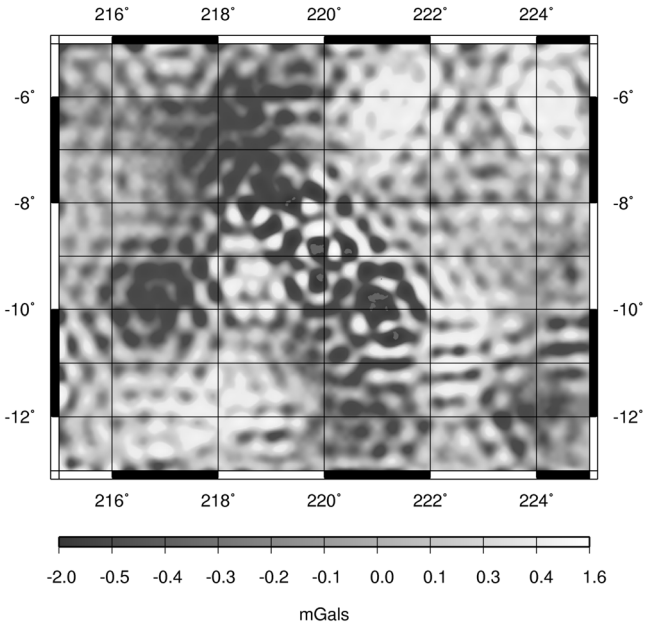

Figure 8. Map of residuals on the gravity anomaly (initial data from KMS 2002 satellite-derived gravity anomalies minus approximated data from 9651 wavelet representation) at 35 km resolution.

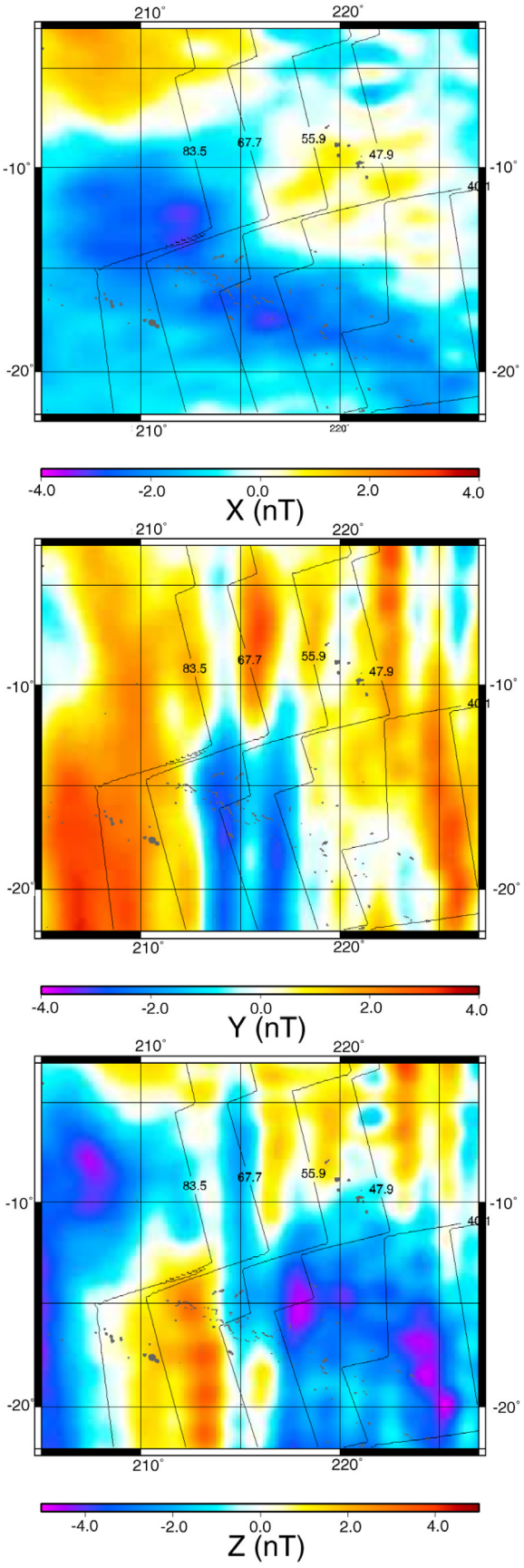

[24] The resulting data set is composed of about 50,000 vector triplets measurements of the magnetic field. The spatial distribution of the data is very dense and corresponds to the full tracks of the CHAMP satellite over the area. In order to reduce the size of the systems to solve, we decimated this data set by selecting one data point out of 10 for each track. This leads to keep about 5,000 vector triplets data, i.e., approximately 8 points per bin of 1 degree per 1 degree.

[25] Since an internal field model was subtracted, the data almost do not contain wavelengths larger than 2700 km. Indeed, the long-wavelength components of the magnetic field are strongly dominated by the core field and at scales smaller than about 2500 km, the magnetic field is mainly due to crustal contributions. Thus the general practice to separate between those two sources is to ignore crustal contributions below degree/order 15, and ignore core components above that limit [*Langel*, 1987]. Moreover, the altitude of the satellite varies between 380 and 480 km. This limits the resolution of our magnetic field model. Our model is finally band limited, due to the nature of the data and the applied corrections.

[26] Last, as the data used result from the difference between the measured magnetic field and a magnetic field model, they correspond to an anomaly field. We will thus compute a wavelet model of the "crustal magnetic anomaly field."

2.4.2. Deriving the Wavelet Representation

[27] The magnetic scalar potential V of the Earth's crustal anomaly field is represented as an infinite superposition of wavelets truncated for practical computations, similarly to the gravity case. The data we use represent the vectorial components X, Y, Z (in local spherical coordinates the northern, eastern, and vertical down component, respectively) of the magnetic field **B**. These components are related to the potential using its negative gradient. In spherical coordinates, this reads

$$\mathbf{B} = \begin{pmatrix} -Z \\ -X \\ Y \end{pmatrix} = \sum_i \alpha_i \begin{pmatrix} -\dfrac{\partial \psi_i}{\partial r} \\ -\dfrac{1}{r}\dfrac{\partial \psi_i}{\partial \theta} \\ -\dfrac{1}{r \sin\theta}\dfrac{\partial \psi_i}{\partial \phi} \end{pmatrix}. \tag{3}$$

This is our observation equation. As previously, the α_i are the coefficients of the linear combination of wavelets representing the magnetic potential.

[28] Table 2 details the set of wavelets used for magnetic field representation. Figure 9 presents the X, Y, and Z components of the magnetic field calculated over the studied area from the discrete wavelet representation. The residuals with respect to CHAMP data used (Figure 10) are comprised between ±1.5 nT which corresponds to the a priori errors on the data. They thus validate our results.

Figure 9. Wavelet representation of the crustal magnetic anomaly field northern X, eastern Y, and downward vertical Z components computed at 400 km altitude; 649 wavelets are used. The thin labeled black lines correspond to the age of the seafloor in Ma determined by *Müller et al.* [1997].

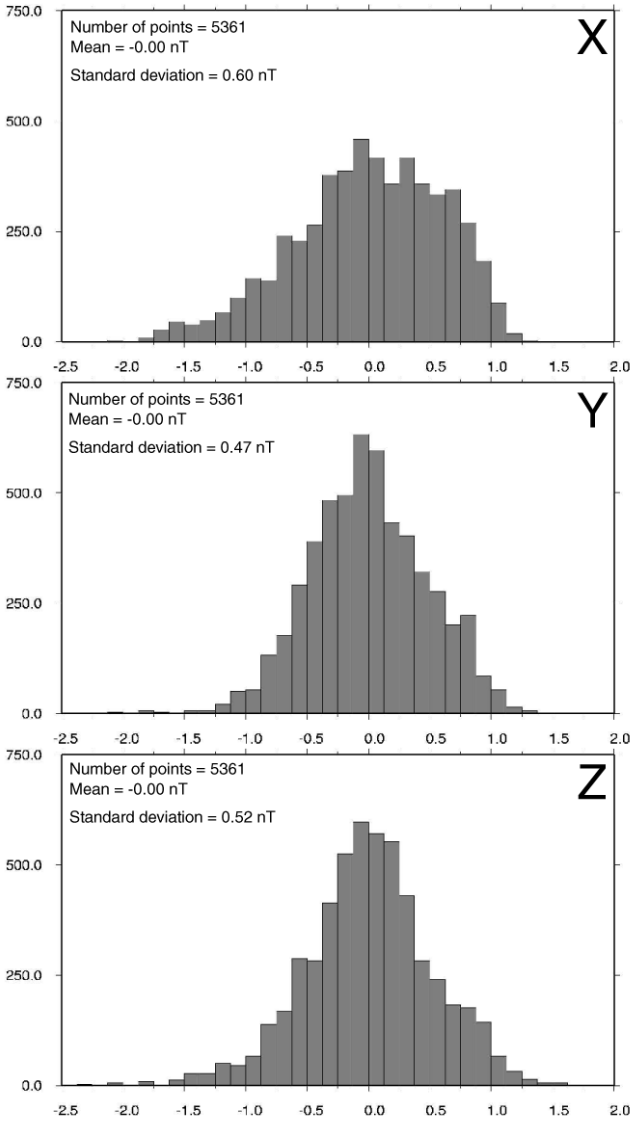

Figure 10. Histogram of residuals on the crustal magnetic anomaly field northern *X*, eastern *Y*, and downward vertical *Z* components (CHAMP data minus approximated data from 649 wavelets representation).

2.4.3. Results

[29] As compared to the classical band-limited spherical harmonics representations of the crustal magnetic field, our magnetic field better represents the fine variations in the magnetic data because of the infinite spectrum of the wavelets. It is consistent with already published crustal magnetic field representations in spherical harmonics [*Maus et al.*, 2002; *Sabaka et al.*, 2004] but shows the advantages of being closer to the data and easier to compute due to the smaller size of the systems to solve.

[30] The magnetic field over the oceans is dominated by the seafloor spreading lineations. These lineations correspond to a remanent magnetization, acquired during the formation of the rocks of the crust and of the upper part of the mantle, as soon as those rocks stay in pressure and temperature conditions below the Curie isotherm. On the eastern *Y* and downward vertical *Z* (Figure 9) components, the lineations are clearly visible, as previously shown by several authors [*LaBrecque and Raymond*, 1985; *Cohen and Achache*, 1994; *Dyment and Arkani-Hamed*, 1998; *Purucker and Dyment*, 2000; *Purucker et al.*, 2003]. In particular, the later isochron of the Cretaceous quiet zone (from about 118 to 83 Ma) is well represented. The comparison between the features observed on Z component and of the digital isochrons grid [*Müller et al.*, 1997] shows a good correlation of larger features.

[31] However, our aim is to study crustal structures other than the lineations. These structures are visible through their induced magnetization, which is proportional to the strength of the ambient field. We think that they should be most visible in the *X* component of the magnetic field for the following reasons. First, the noise of the data is better removed along-track, that is to say in the *X* direction since the CHAMP satellite follows a nearly polar orbit. Second, the seafloor spreading lineations in our area trend roughly in the north-south direction and should thus be mostly visible in the transverse (*Y* and *Z*) components of the magnetic field. Therefore the *X* component should be less affected by both noise and lineations. It should also be more sensitive to roughly east-west structures such as fracture zones. We thus conclude that we should study the *X* component of the magnetic field in this area in order to detect any magnetic anomaly associated to structural heterogeneities in the oceanic crust.

[32] Figure 9 shows a very clear magnetic anomaly that does not resemble a lineation in the *X* component map. This map differs from the *Y* and *Z* components maps, more influenced by the lineations. We observe a large anomaly on the *X* component, centered on the Tuamotu chain. It is inverse to the ambient field and appears in blue on Figure 9. Its orientation is N60°W. By inference, this anomaly reflects structural heterogeneities of the crust, as discussed in section 4.

3. Analysis of the Gravity Field: Continuous Wavelet Transform

3.1. When to Apply a Continuous Wavelet Analysis?

[33] We now analyze our thus obtained gravity field in order to characterize its behavior at different spatial resolutions. Let us recall that, because of the presence of many spatial scales in the gravity field in this area, filtering has often been applied in order to characterize the geological structures at different scales in this area. Here we choose to apply a continuous wavelet analysis (CWT) on the sphere.

[34] Let us recall the differences between the discrete wavelet representations and the continuous wavelet analysis. The discrete wavelet representations are well suited to compute a gravity or magnetic field representation from various data sets, but the coefficients of the wavelet representation are not defined as correlation coefficients between the measured potential and the wavelets representing it. They may be nonunique. This comes from the fact that the wavelet set is not an orthonormal basis but a frame. Consequently, those coefficients are difficult to interpret, and thus the discrete wavelet representation is only aimed at representing the data.

[35] On the contrary, the continuous wavelet transform is made of a set of analysis coefficients $C_{a,e}$ at different scales

a and positions e which are defined as the correlations between a wavelet of given scale and position and the potential. Moreover, the sampling of scales and positions is extremely fine (it is continuous, as opposed to the discrete sampling of the discrete wavelet representation). The continuous wavelet transform is thus an appropriate tool to analyze the gravity potential at different spatial scales. The reader interested in the continuous wavelet transform from a more general point of view is referred to *Holschneider* [1995].

[36] Finally, when using Poisson multipole wavelets, we will show that the coefficients of the CWT give an integrated, weighted view of the anomalous density distribution. Note that Poisson wavelets are also used in one or two dimensions (in the planar case) to analyze the sources of potential fields anomalies [*Moreau et al.*, 1999; *Martelet et al.*, 2001; *Sailhac and Gibert*, 2003].

3.2. Computation of the CWT on the Sphere

[37] The CWT coefficients are defined as the correlations between a wavelet of given scale and position and the potential. They may be written as

$$C_{a,e} = \left\langle \psi_a^{m,e}, V \right\rangle, \tag{4}$$

where angle brackets denote the usual scalar product on the sphere S given by $\langle x, y\rangle = \int_S xyd\sigma$; and $\psi_a^{m,e}$ is a wavelet of scale a, order m and position e; and V is the potential represented as an infinite superposition of discrete wavelets:

$$V = \sum_{a',e'} \alpha_{a'}^{e'} \psi_{a'}^{m',e'}. \tag{5}$$

The scalar product from equation (4) may thus be written as

$$C_{a,e} = \sum_{a',e'} \alpha_{a'}^{e'} \left\langle \psi_{a'}^{m',e'}, \psi_a^{m,e} \right\rangle. \tag{6}$$

In practice, these infinite sums will always be truncated, as previously mentioned. The interesting point when using Poisson multipole wavelets is that the correlation between two wavelets is actually equal to another Poisson multipole wavelet, of different order, evaluated at a specific point [*Holschneider et al.*, 2003]. Thus we get

$$C_{a,e} = \sum_{a',e'} \alpha_{a'}^{e'} \frac{a^m a'^{m'}}{(a+a')^{m+m'}} \psi_{a+a'}^{m+m',e'}(e). \tag{7}$$

The coefficients $\alpha_{a'}^{e'}$ are fixed once the discrete wavelet representation is computed, and the CWT on the sphere can be derived.

3.3. Link With Density Distribution

[38] Now we investigate how the CWT coefficients are related to the underlying anomalous density distribution. V stands for the Earth's gravity potential anomaly, and $\delta\rho$ is the anomalous density distribution inside the Earth of volume V_E, comprised inside the sphere S_R of radius R. One has

$$V(\mathbf{y}) = G \int_{V_E} \frac{\delta\rho(\mathbf{x})}{|\mathbf{y}-\mathbf{x}|} d\Omega(\mathbf{x}). \tag{8}$$

The CWT coefficients $C_{a,e}$ are given by

$$C_{a,e} = \int_{S_R} V(\mathbf{y}) \psi_a^{m,e}(\mathbf{y}) d\Sigma(\mathbf{y}). \tag{9}$$

The wavelet $\psi_a^{m,e}$ may be expanded as a series of Legendre polynomials P_ℓ [*Holschneider et al.*, 2003]:

$$\psi_a^{m,e}(\mathbf{y}) = \frac{a^m}{|\mathbf{y}|} \sum_\ell \ell^m \left(\frac{|\mathbf{e}|}{|\mathbf{y}|}\right)^\ell Q_\ell(\hat{\mathbf{e}}\cdot\hat{\mathbf{y}}), \tag{10}$$

where $|\mathbf{e}| = R\exp(-a)$ and $Q_\ell = ((2\ell+1)/4\pi)\,P_\ell$. We use the notation $\hat{\mathbf{y}} = \mathbf{y}/|\mathbf{y}|$. We substitute (8) into (9). Taking into account the Legendre expansions of $\psi_a^{m,e}$ and of $1/|\mathbf{y}-\mathbf{x}|$ (see Appendix A) and the orthogonality relations between Legendre polynomials, yields

$$C_{a,e} = Ga^m \int_{V_E} \delta\rho(\mathbf{x}) F_a^{m,e}(\mathbf{x}) d\Omega(\mathbf{x}), \tag{11}$$

with

$$F_a^{m,e}(\mathbf{x}) = \sum_\ell \ell^m |\mathbf{e}|^\ell |\mathbf{x}|^\ell P_\ell(\hat{\mathbf{e}}\cdot\hat{\mathbf{x}}). \tag{12}$$

Here we work on the unit sphere to simplify the expressions. Thus the CWT coefficients are the integral of anomalous densities with a weighting function $F_a^{m,e}$. This weighting function may be written in a more compact form by classical identification of the Legendre series with a multipolar development:

$$F_a^{m,e}(\mathbf{x}) = \left(|\mathbf{e}|\delta_{|\mathbf{e}|}\right)^m \left(\frac{1}{|\mathbf{x}|}\frac{1}{\left|\frac{\mathbf{x}}{|\mathbf{x}|^2} - \mathbf{e}\right|}\right). \tag{13}$$

The necessary condition $|\mathbf{x}| < 1/|\mathbf{e}|$ is always verified when $\mathbf{x}$ is inside the sphere and $|\mathbf{e}| < 1$. Because of the symmetry of the Legendre expansion of $F_a^{m,e}$, the weighting function admits in fact several equivalent analytical formulations, for instance,

$$F_a^{m,e}(\mathbf{x}) = \left(|\mathbf{e}|\delta_{|\mathbf{e}|}\right)^m \left(\frac{1}{|\mathbf{e}|}\frac{1}{\left|\mathbf{x} - \frac{\mathbf{e}}{|\mathbf{e}|^2}\right|}\right). \tag{14}$$

Thus the weighting function is actually a multipole centered outside the sphere, symmetrically to the wavelet itself. Figure 11 shows a cross section of this function for an order 3 Poisson multipole wavelet located at radius $r = 3800$ km inside the Earth. It is mainly localized in latitude/longitude at the position of the wavelet, and has a penetration depth inside the sphere which is proportional to the wavelet scale.

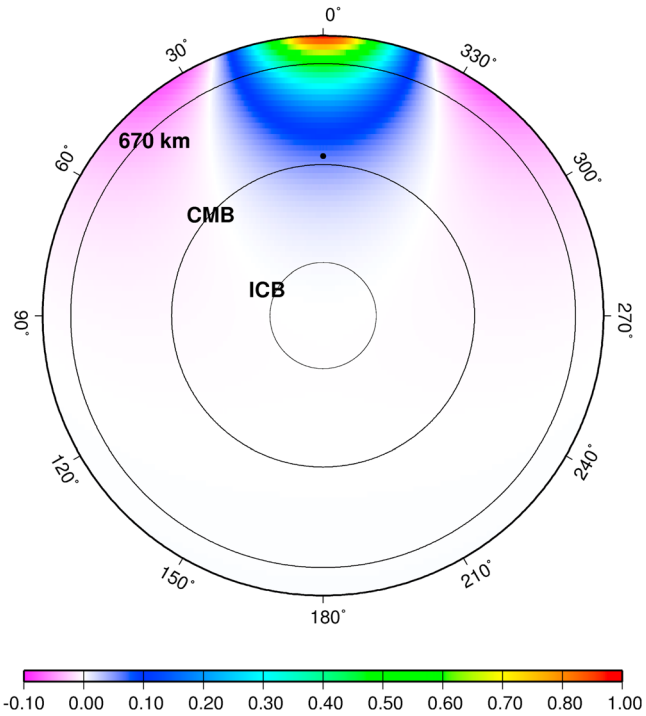

Figure 11. Weighting function $F_a^{m,e}$ of internal densities for an order 3 Poisson multipole analyzing wavelet at radius r = 3800 km inside the Earth.

This reflects the well-known fact for potential fields that a given wavelength corresponds to a maximum penetration depth inside the Earth.

3.4. Description of the CWT of Gravity Field

[39] Animation S1 in the auxiliary material[1] shows the results of the CWT of our gravity field. Each image corresponds to the CWT of the gravity potential at a given spatial scale a (in yellow). On the left side of the images, we represent the weighting function $F_a^{m,e}$ of the densities inside the Earth, with the same color scale as on Figure 11. On the right side of the images, we represent the coefficients $C_{a,e}$ of the CWT of the gravity potential at the considered scale a and for all positions e. As the geoid N is simply related to the gravity potential T through the Bruns equation [*Moritz*, 1989]: $N = T/\gamma$ (where γ is the normal gravity), these coefficients actually image the characteristics of the geoid at different wavelengths. We selected a few images from Animation S1: they are shown on Figure 12 and on the top left of Figure 13 (the weighting function is, however, not shown on these figures).

[40] The already known features of this area are well displayed by the CWT. This validates our approach. For instance, at large scale, we recognize the well-known geoid low (see analysis map at 1090 km scale and also at larger scales in Animation S1). This geoid low, already discussed by *McNutt and Judge* [1990], is associated to the Superswell bathymetric high [*McNutt and Fischer*, 1987] and to slow seismic velocities in the upper and lower mantle [*Ekström and Dziewonski*, 1998; *Gu et al.*, 2001; *Romanowicz and Gung*, 2002]. We also image the geoid high associated to the Marquesas islands, shifted with respect to the axis of the chain, as mentioned by *Filmer et al.* [1993]. This geoid high consists of two anomalies visible at 290 (see Animation S1) and 256 km scale. The first one is an elongated maximum shifted in a northeast direction with respect to the Marquesas Islands, and the second one is superimposed to the islands chain [*Adam et al.*, 2005]. We image the geoid undulations trending about N110°E at 200 km and lower scales in the southeastern part of the area, in agreement with previous observations from satellite altimetry [*Haxby and Weissel*, 1986; *Baudry and Kroenke*, 1991; *Maia and Diament*, 1991; *Cazenave et al.*, 1992; *Fleitout and Moriceau*, 1992; *Wessel et al.*, 1994].

[41] Apart from these already known characteristics, the continuous wavelet analysis brings out new structures in the gravity field. The most striking one is the different gravity signatures of the islands chains. The Society chain is associated with a strong positive geoid anomaly at all scales. Moreover, this anomaly surprisingly contains very large scale components (see the analysis map at 1090 km scale). The geoid high over the Marquesas chain has a smaller amplitude and no component at scales larger than about 750 km. The geoid signature of the Cook-Austral chain is less clear because it limits the large geoid low of French Polynesia. A large-scale, a positive anomaly might be associated to the southern Australs, where active volcanism takes place, but part of the curved anomaly, as seen on the 705 km scale map, is not correlated with the bathymetry.

[42] We also discover new features on a lithospheric scale. At 256 km, the geoid anomaly associated with the Marquesas chain shows a strikingly sharp limit on its southwestern edge, parallel to the chain. We observe at 200 km scale and less, the structural direction N45°E north and south of the Marquesas Islands. These directions delimit a rectangular, negative geoid anomaly crossing the Marquesas fracture zone. It encloses the Marquesas at the northeast edge, and it is limited by the Tuamotus Islands at the southwest edge. We also point out the very asymmetric shape of the flexural geoid low around the Marquesas, parallel to the chain, at scales 200 km and smaller. This flexural low also shows a very geometric shape. Last, the wavelet analysis at 37 km scale around the Marquesas shows a clear link between the volcanic edifices of the Marquesas Fracture Zone, west of the islands, and Fatu-Hiva island, where the most recent volcanic activity was reported by *Jordahl et al.* [1995].

3.5. CWT of the Gravity Effect of the Bathymetry

[43] To separate superficial from deeper processes when interpreting the gravity analysis maps, we now estimate the contribution from the bathymetry in the continuous wavelet analysis. We use a compilation of bathymetric data from ship sonar measurements from *Adam and Bonneville* [2005]. In this compilation, data are interpolated in between the tracks using spline interpolation. The resulting grid covers the area comprised between longitudes 190°E and 230°E, and between latitudes 20°N and 35°S.

[44] We directly derive the CWT of the gravity effect of the bathymetry. The principle of the calculation is the same as for the gravity field analysis. We first compute a discrete

[1] Auxiliary materials are available in the HTML. doi:10.1029/2005jb004141.

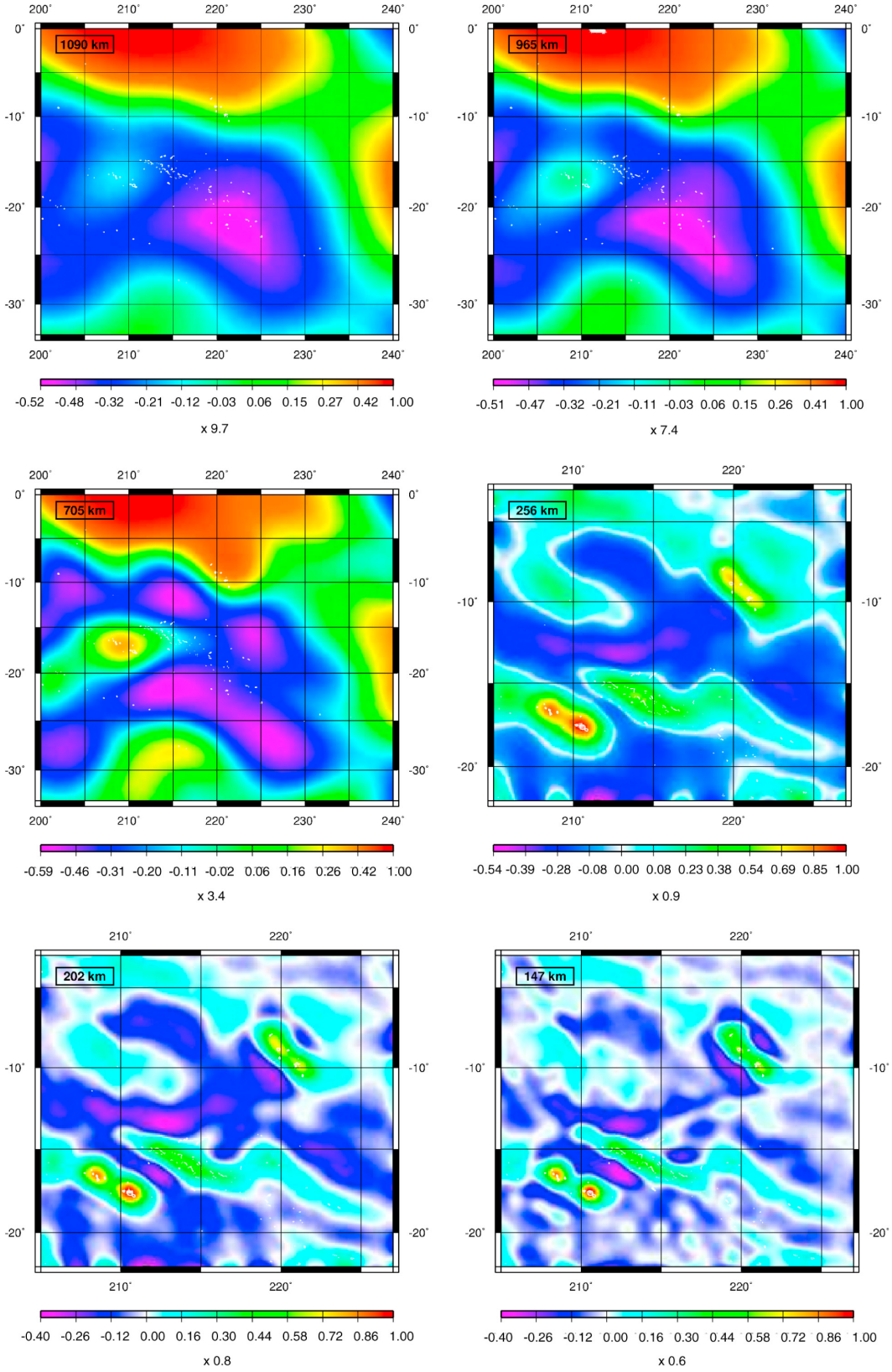

Figure 12. Continuous wavelet analysis of the gravity potential anomaly in French Polynesia: map of analysis coefficients at varying scales, from 1090 to 147 km. The coefficients have dimensions of $m^2\ s^{-2}$.

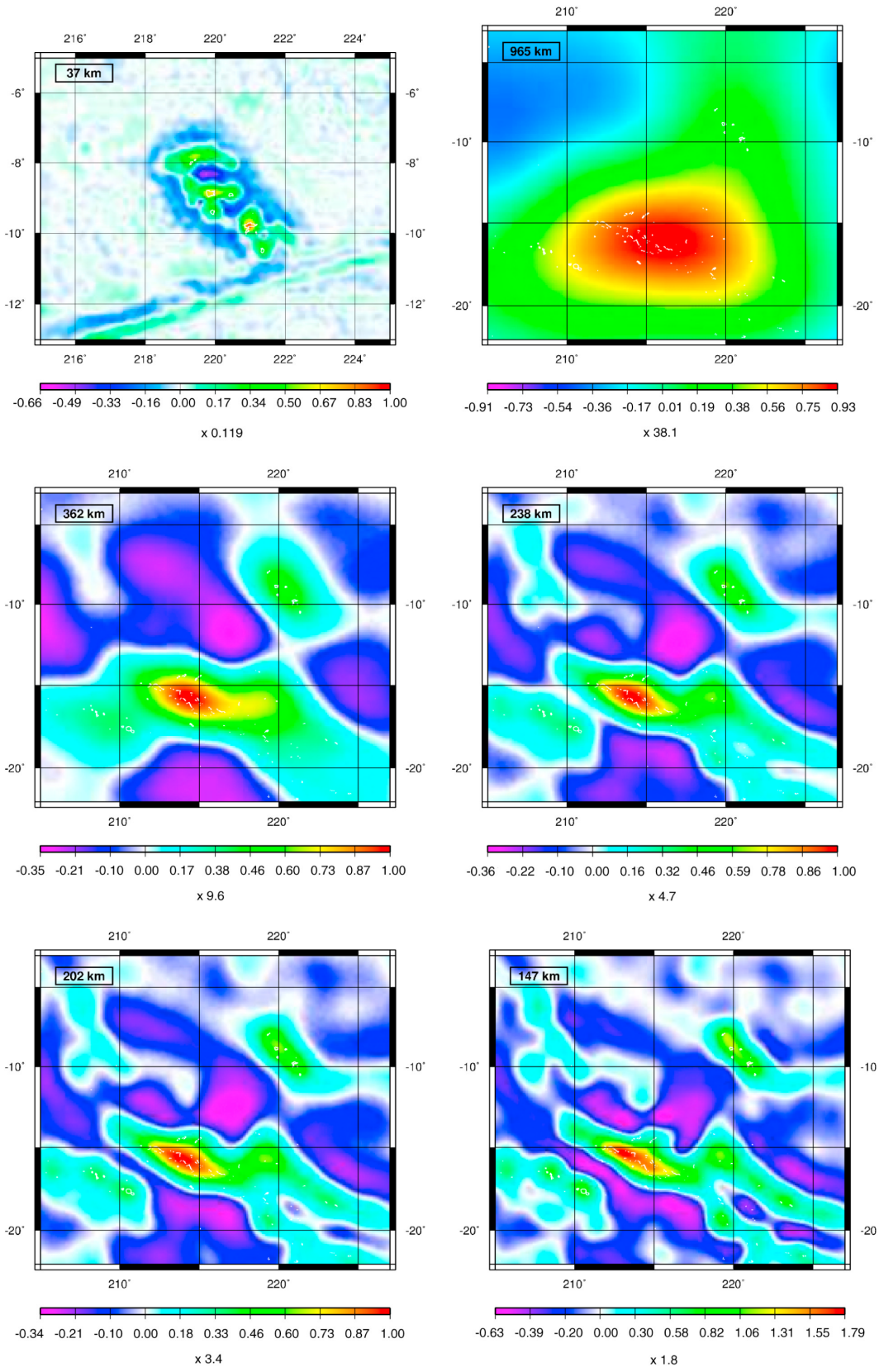

Figure 13. Top left image, continuous wavelet analysis of the gravity potential anomaly around the Marquesas at 37 km scale. Other images, continuous wavelet analysis of the gravity potential anomaly in French Polynesia due to the bathymetry: map of analysis coefficients at varying scales, from 965 to 147 km. The coefficients have dimensions of $m^2\ s^{-2}$.

wavelet representation of the bathymetric data, and then derive the CWT of the gravity effect of the bathymetry as explained in Appendix A. Animation S2 in the auxiliary material shows the resulting analysis maps. Each image corresponds to the CWT of the gravity potential of bathymetric origin at a given spatial scale a (in yellow). We represent the coefficients $C_{a,e}$ of the CWT of the gravity potential of the bathymetry at the considered scale a and for all positions e. We again selected a few images from Animation S2, shown on Figure 13.

[45] The comparison between the CWT of the total gravity field and the CWT of the bathymetric contribution again underlines the differences between the islands chains: Whereas we observe in the Tuamotu region a large bathymetric contribution and a weak gravity signature in the CWT of the total gravity field, the Society Islands show the opposite behavior. In the Marquesas chain, we notice the geometric shape of the bathymetric contribution at scale 362 km.

4. Discussion

[46] Now we discuss the origin of intraplate volcanism in south central Pacific on the basis of our results from the wavelet representation and analysis of potential fields.

4.1. General Structure of the Crust From Magnetic Anomalies

[47] Our high-resolution representation of the crustal magnetic anomaly field over French Polynesia at 400 km altitude shows the largest features of the crust structure. Indeed, we interpret our anomaly in the northern magnetic field component as reflecting the crustal thickening of the Tuamotu plateau. Forward models confirm this interpretation. For example, *Cohen and Achache* [1990, 1994] show the same feature above Tuamotu when considering only the induced magnetization due to the distribution of seafloor topography and its isostasic compensation. This confirms the fact that the Tuamotu plateau has been emplaced on ridge [*Talandier and Okal*, 1987].

[48] If the crustal magnetic anomaly field does not reflect deeper structures, let us recall that the Pacific area is an intriguing region when considering the main magnetic field. It presents an anomalously low secular variation [*Walker and Backus*, 1996; *Merrill et al.*, 1998; *Jackson et al.*, 2000]. Authors also agree on the fact that the center of the Pacific area might display a main geomagnetic field influenced by the hot underlying lower mantle. Indeed, modification of core flow due to lateral variations in temperature in the core-mantle boundary region of the lower mantle might affect the geodynamo and thus the observed magnetic field [*Johnson and Constable*, 1998].

4.2. General Gravity Signature of the Island Chains

[49] A positive geoid (or gravity) anomaly may be explained by an excess of mass, or by a buoyant upwelling that deforms the interface of densities. The interfaces deflection strongly depends on the viscosity profile of the mantle. To the contrary, a negative geoid anomaly may result from a deficit of mass, or a buoyant upwelling that does not deform the superficial interfaces because of the presence of a low-viscosity zone. Thus the geoid effect of a density anomaly at depth will strongly depend on the viscosity profile of the mantle: The way a density anomaly at a given depth influences the geoid at a given wavelength is described by the so-called geoid kernels [*Hager et al.*, 1985; *Forte and Peltier*, 1991]. If equilibrium is attained, the excess mass of the seafloor topography is compensated by an equal mass deficit at depth, thus resulting in a positive geoid anomaly which amplitude depends on the depth of the mass deficit. For instance, the weak gravity signature of the Tuamotu plateau is due to the very superficial compensation by a crustal thickening.

[50] In the absence of any deeper density anomaly, similar topographic loads emplaced on a crust of comparable rigidity should lead to similar gravity signatures. Here, this is clearly not the case:

[51] 1. At large scales (about 1100 km), the most striking feature in the CWT of the gravity field is the clear positive anomaly associated to the Society Islands. This anomaly persists in a wide range of spatial scales. This strong positive anomaly over the Society area indicates a deeper support of the Society swell, or a more important bathymetric load for the Society chain than for the other chains.

[52] 2. The Cook-Austral chain is marked by two swells [*Adam et al.*, 2005] that we clearly recognize in the CWT of the bathymetric contribution. The very large scale (1100 km) positive anomaly over the southeastern part of the chain could indicate a deeper support of the swell than for the swell at the western end of the chain, which is associated with a weaker gravity anomaly. However, the gravity anomaly in the southern part of the chain is rather puzzling. Indeed, at 705 km scale, it shows a curved shape and part of the anomaly has no bathymetric expression. The presence of an anomaly without any bathymetric expression in the vicinity of a volcanic chain was also observed in the Marquesas chain [*Adam et al.*, 2005]. It indicates the presence of a load at depth, but further studies are necessary to better understand its origin. We may conclude that it underlines the well-known complexity of the Cook-Austral chain [*Turner and Jarrard*, 1982; *Diament and Baudry*, 1987].

[53] 3. A rather superficial support of the Marquesas swell seems probable given the weak gravity signature at very large scales, consistent with the presence of underplated material [*Caress et al.*, 1995; *McNutt and Bonneville*, 2000].

[54] Such different behaviors of the different volcanic chains indubitably establish that the processes originating the Polynesian volcanism differ from one island chain to the other. We will now detail the cases of the Society and Marquesas chains. For the Cook-Austral chain, it is necessary to carry out further studies at smaller scale (our CWT only images the large scales of the Cook-Austral gravity field).

4.3. Society Islands

[55] To interpret the gravity signature of the Society chain, we first test the hypothesis of a strong bathymetric contribution. The wavelet analysis of the gravity effect of the bathymetry does not show any specific feature over the Society area at 940 km scale, whereas at that scale, the observed geoid over the Society already shows a clear positive anomaly. Moreover, the flexure of the crust under

the Society topography should create a negative geoid anomaly, and not a positive one. Thus we conclude that the gravity signature of the Society chain at larges scales cannot be explained by the effect of the seafloor topography and the corresponding flexure of the crust.

[56] On the basis of these observations, the geoid anomaly over the Society chain is abnormally strong. This probably indicates a deeper dynamic support of the Society chain. Such an hypothesis is consistent with other elements from seismological investigation. Indeed, *Niu et al.* [2002] evidenced a 25 km thinning of the transition zone in an area 500 km or less in diameter below the Society chain. This thinning is associated to a temperature increase in the mantle possibly due to the presence of a hot rising plume. *Niu et al.* [2002] also note a normal transition zone thickness elsewhere in the Superswell. We thus computed the gravity and geoid effects of a 500 km wide, 25 km thinning of the transition zone. Depending on the distribution of interfaces deflection at the base and at the summit of the transition zone, we may generate gravity anomalies of varying amplitudes. For instance, a 12.5 km deflection of both interfaces, with a density contrast of -0.1 at the top and 0.4 at the bottom, according to PREM model [*Dziewonski and Anderson*, 1981], produces a 1000 km wide gravity anomaly of maximum amplitude equal to 7 mGal, at sea surface. We tested different distributions of deflections, always keeping a maximum amount of 25 km deflection in a 500 km wide deflected area. The amplitude of the produced gravity signal may vary (and notably increase), but its spatial extent always amounts to about 1000–1200 km. The corresponding effect on the geoid is about 1 m, over a 1000–1200 km wide area. Such characteristics are consistent with the results of the wavelet analysis. We also bring constraints on the geometry of the transition zone thinning since a too strong deflection of the 410 km limit would induce a negative geoid anomaly, that is not observed here. Our oversimplified model does not take into account the interfaces deflections between the transition zone and the surface, which depend on the local viscosity profile. Such deflections could explain that the anomalous gravity behavior of the Society chain persists at all spatial scales down to 100 km. Thus we conclude that the gravity signature of the Society Islands is coherent with the hypothesis of a deeply anchored plume under the Society Islands. Further work is necessary to better characterize the geometry of this upwelling, and to precisely quantify the transition zone thinning. To that aim, a joined inversion of inversion of seismic data with the present wavelet analysis would be very useful but is out of the scope of this paper.

4.4. Marquesas Islands

[57] We first note that the Marquesas islands are located on top of a geoid undulation. Such undulations, oriented N120°E, clearly show up at 200 km scale. For instance, a large, negative one crosses the whole area, just north of the Tuamotu chain. A smaller one is also visible at 180 km scale, south of the ridge of the Marquesas Fracture Zone. The Marquesas chain is located in the continuation of one of these undulations, as shown on the analysis map at 147 km scale. This geoid undulation is associated with an undulation of bathymetric origin, as shown in the analysis map of the bathymetry at 147 km scale. Moreover, the flexural geoid low of the Marquesas islands does not seem to be located all around the Marquesas archipelago, but preferentially southwest and northeast of the islands, i.e., on both sides of the geoid undulation and not across it. Therefore we illustrate the fact that the Marquesas chain is emplaced on a geoid undulation the origin of which remains a matter of debate, associated with a bathymetric undulation. On the basis of the very different gravity signatures of the Marquesas and Society chains, we favor a superficial origin for this undulation rather than a deep hot spot track hypothesis. A plausible explanation is that of secondary convection rolls, as invoked by *Maia and Diament* [1991] to explain geoid anomalies in French Polynesia. This secondary convection would result from the existence of a thermal gradient and a low-viscosity zone at the base of the lithosphere [*Richter*, 1973; *Yuen and Fleitout*, 1984; *Robinson and Parsons*, 1988].

[58] Second, the Marquesas islands are located in a strikingly rectangular geoid low limited by the Tuamotu plateau. This low trends N45°E, and is visible in the analysis map at 200 km scale. We do not clearly detect this feature in the CWT of the bathymetric contribution. However, the bathymetric grid is less reliable there since cruises are sparse in this zone. According to its sharp geometry, this geoid low probably reflects structural heterogeneities in the lithosphere. Its shape calls for two comments. The first one is that the N45°E direction has been already noticed in the area. Focal mechanisms in French Polynesia [*Okal et al.*, 1980] delineate the N45°E direction as a Riedel shear orientation, reflecting the regional stress of the lithosphere, and conjugated to the N120°E direction. The authors interpret this stress field as the stress deviator imposed by the system of plate tectonic driving forces, underlining the importance of the ''ridge-push'' effect. *Binard et al.* [1991] also report the N40°E direction at the scale of a volcano edifice in the Society area. Thus the geoid anomaly we detect could indicate a possible control of the Marquesian volcanism by N45°E fracturation linked to the regional stress of the lithosphere. The second comment is that the rectangular geoid low seen at 200 km scale seems to establish a link between the Marquesian and Tuamotu chains. Moreover, in several cases, off-ridge volcanism is emplaced in the close vicinity of an on-ridge plateau leading to a polyphase formation of the relief. This raises the question of how these plateaus modify the surrounding lithosphere and the underlying mantle. *Ito et al.* [1995] propose that the Tuamotu plateau could result from the interaction between a propagating rift and a hot spot close to the ancient Pacific/Farallon spreading center, 50 Myr ago. This propagating rift must have initiated close to the ancient Marquesas Transform Fault. Thus the whole lithosphere might have been weakened in the vicinity of the Tuamotu chain enclosing the actual location of the Marquesas Islands. It is of particular interest to note that the N45°E direction is compatible with the direction of the outer pseudofault associated to the propagating rift. The question of how this rift propagation could have interfered with the transform fault remains open. The recent hot spot volcanism would then have been preferentially driven in the weakened area.

[59] Finally, the positive geoid anomaly associated to the Marquesas chain at 256 km scale has a very sharp limit,

southwest of the chain, parallel to the chain. The bathymetric contribution, reflecting the Marquesas apron, shows a geometric shape at about 360–240 km scales, such as the flexural geoid low at scales smaller than 200 km. All these observations again indicate a strong lithospheric control on the Marquesian volcanism. A fault oriented N140° may originate the sharp geoid limit at 256 km scale. The geometric shapes of the flexure and of the apron may result from crustal discontinuities and fracturation. Further studies are necessary to fully comprehend these observations, but they clearly underline the complexity of the area and the primary role of the lithospheric control on the volcanism.

5. Conclusion

[60] In this paper, we implement a wavelet representation of potential fields in French Polynesia that allows to combine heterogeneous data sets. We apply this method to refine a global, ''low''-resolution gravity field with local, high-resolution data, leading to a combined gravity field in French Polynesia. We also derive a crustal magnetic field representation from CHAMP data.

[61] The magnetic field images the general, large-scale characteristics of the crust. We observe the crustal thickening associated to the Tuamotu plateau, in agreement with previous results from seismic investigation.

[62] The gravity field mainly images the different islands chains and how they are supported. To isolate the contributions at the different spatial scales, it is necessary to apply a filtering. To that aim, we compute the continuous wavelet analysis of the gravity field. We moreover show that the coefficients of the wavelet analysis provide an integrated, weighted view of the internal distribution of densities.

[63] Our analysis brings to light many features in this area.

[64] 1. We show that the gravity signature of the islands chains considerably differs from one chain to another. We then confirm that different processes must be invoked to explain the Polynesian volcanism.

[65] 2. We show that the Society Islands are marked by a strong positive gravity anomaly at all scales and especially at very large scale. This anomaly may not be explained at large scale by the effect of the bathymetry and probably mirrors a deep dynamic support of the swell. We interpret it as the signature of a deep plume under the Society Islands.

[66] 3. We show that the gravity anomalies associated to the Cook-Austral swells are more important for the southern swell than for the northern one. Deep processes may be at stake at the southern end of the chain, where active volcanism takes place. Further studies at smaller scales are, however, necessary to precise and fully understand our observations.

[67] 4. We show that the Marquesian volcanism may be influenced by superficial processes such as secondary convection, and must be controlled by lithospheric weaknesses due to the regional stress of the Pacific plate or the influence of the Tuamotu plateau.

[68] Finally, such wavelet methods appear to be very powerful and are well suited to represent and analyze the existing and future satellite gravity and magnetic data, in particular from the future Gravity Field and Steady-State Ocean Circulation Explorer (GOCE) and Swarm missions. Joined inversions of wavelet analysis of potential fields with seismology should bring valuable insights into the Earth's structure and dynamics.

Appendix A: CWT of the Gravity Effect of a Bathymetric Load

[69] The wavelet analysis coefficients of the gravity effect of a bathymetric load are computed in two steps. First, we compute a discrete wavelet representation of the bathymetric data. Second, we derive the continuous wavelet analysis.

A1. Discrete Wavelet Representation

[70] We apply the same method as described for potential field representation. The difference lies in the fact that here, we only consider a scalar function on a sphere, corresponding to the bathymetric depths b. This scalar function is written as a superposition of wavelets:

$$b = \sum_{a,e} \alpha_a^e \psi_a^{m,e}. \tag{A1}$$

We solve a least squares inversion to derive the coefficients α_a^e as explained by *Chambodut et al.* [2005] in the case of a scalar function. Thus we obtain a discrete wavelet representation of the bathymetric depths.

A2. CWT

[71] Now we want to derive the wavelet analysis of the gravity effect of the bathymetry. For that aim, we follow the approach of Wahr et al. written in the spherical harmonics case [*Wahr et al.*, 1998] and adapt it to the case of the Poisson multipole wavelets. Note that this approach is similar to the one of *Fengler et al.* [2005].

[72] Let us consider the gravity potential of a bathymetric load V_b of constant density ρ, equal to the difference between density of the oceanic crust and density of the water (1700 kg m^{-3}):

$$V_b(\mathbf{y}) = \int_{\mathbf{x}\in\text{bathymetry}} \frac{G\rho(\mathbf{x})}{|\mathbf{y}-\mathbf{x}|} d\Omega(\mathbf{x}). \tag{A2}$$

The wavelet analysis coefficient C_a^e of V_b is given by

$$C_a^e = \langle V_b, \psi_a^{m,e} \rangle, \tag{A3}$$

which is equal to

$$C_a^e = \int_{\mathbf{y}\in S_R} \int_{\mathbf{x}\in\text{bathymetry}} \frac{G\rho(\mathbf{x})}{|\mathbf{y}-\mathbf{x}|} \psi_a^{m,e}(\mathbf{y}) d\Sigma(\mathbf{y}) d\Omega(\mathbf{x}), \tag{A4}$$

with S_R the surface of the sphere enclosing all masses.

[73] We now introduce the Legendre series expansion of the following functions:

$$\frac{1}{|\mathbf{y}-\mathbf{x}|} = \frac{1}{|\mathbf{y}|} \sum_\ell \left(\frac{|\mathbf{x}|}{|\mathbf{y}|}\right)^\ell P_\ell(\hat{\mathbf{x}}\cdot\hat{\mathbf{y}}), \tag{A5}$$

and

$$\psi_a^{m,e}(\mathbf{y}) = \frac{a^m}{|\mathbf{y}|} \sum_\ell \ell^n \left(\frac{|\mathbf{e}|}{|\mathbf{y}|}\right)^\ell Q_\ell(\hat{\mathbf{e}}\cdot\hat{\mathbf{y}}). \tag{A6}$$

Substituting equations (A5) and (A6) into equation (A4) and taking into account the orthogonality relations between Legendre polynomials, we end up with

$$C_a^e = \int_{x\in\text{bathymetry}} \frac{a^m G\rho(\mathbf{x})}{|\mathbf{y}|^2} \sum_\ell \ell^n \left(\frac{|\mathbf{e}|}{|\mathbf{y}|}\right)^\ell \left(\frac{|\mathbf{x}|}{|\mathbf{y}|}\right)^\ell P_\ell(\hat{\mathbf{x}}\cdot\hat{\mathbf{e}}) d\Omega(\mathbf{x}). \tag{A7}$$

Exchanging the integral and the discrete sum, we derive

$$C_a^e = \frac{Ga^m}{|\mathbf{y}|^2} \sum_\ell \ell^n \int_{\mathbf{x}\in\text{bathymetry}} \rho(\mathbf{x}) \left(\frac{|\mathbf{e}|}{|\mathbf{y}|}\right)^\ell \left(\frac{|\mathbf{x}|}{|\mathbf{y}|}\right)^\ell P_\ell(\hat{\mathbf{x}}\cdot\hat{\mathbf{e}}) d\Omega(\mathbf{x}). \tag{A8}$$

We now apply the hypothesis of thin layer. Suppose that all bathymetric masses are enclosed in a layer of maximum thickness $H_{\max}$ comprised between the spheres of radius R and $R - H_{\max}$. We can write $(|x|/|y|)^\ell \approx 1$ if $\ell(H_{\max}/R) \ll 1$. For instance, 150 km resolution corresponds to $\ell = 133$ and the thin layer approximation applies if $H_{\max} \ll 48$ km. In south central Pacific, this constraint is satisfied. Equation (A8) thus simplifies to

$$C_a^e \approx \frac{Ga^m}{|\mathbf{y}|^2} \sum_\ell \ell^n \int_{S_R} \left(\int_{R-H(\hat{\mathbf{x}})}^R \rho dr\right) \left(\frac{|\mathbf{e}|}{|\mathbf{y}|}\right)^\ell P_\ell(\hat{\mathbf{x}}\cdot\hat{\mathbf{e}}) d\Sigma(\mathbf{x}). \tag{A9}$$

Let us introduce the surfacic load $\Delta\Sigma(\hat{\mathbf{x}}) = \int_{R-H(\hat{\mathbf{x}})}^R \rho dr$. We finally have

$$C_a^e \approx \frac{Ga^m}{|\mathbf{y}|^2} \sum_\ell \ell^n \left(\frac{|\mathbf{e}|}{|\mathbf{y}|}\right)^\ell \int_S \Delta\sigma(\hat{\mathbf{x}}) P_\ell(\hat{\mathbf{x}}\cdot\hat{\mathbf{e}}) d\Sigma(\mathbf{x}), \tag{A10}$$

which may be written as

$$C_a^e \approx \frac{G}{|\mathbf{y}|} \langle \Delta\sigma, a^m F^{m,e} \rangle, \tag{A11}$$

with the function $F^{m,e}$ defined as

$$F^{m,e}(\mathbf{x}) = \frac{1}{|\mathbf{y}|} \sum_\ell \ell^m \left(\frac{|\mathbf{e}|}{|\mathbf{y}|}\right)^\ell P_\ell(\hat{\mathbf{x}}\cdot\hat{\mathbf{e}}). \tag{A12}$$

[74] Now, we will explain how to compute the scalar product $\langle \Delta\sigma, F^{m,u} \rangle$. As the densities are supposed to be constant, function $\Delta\sigma$ is simply proportional to the bathymetry. Thus we may write

$$\Delta\sigma = \rho \sum_{a',e'} \alpha_{a'}^{e'} \psi_{a'}^{m,e'}. \tag{A13}$$

We insert equations (A12) and (A13) into equation (A11), we use the Legendre series expansion of the wavelets and the orthogonality relations between the Legendre polynomials to derive finally

$$(\Delta\sigma, F^{m,e}) = \sum_{a',e'} \alpha_{a'}^{e'} \frac{a'^m}{|\mathbf{z}|^2} \sum_\ell \ell^{2m} \left(\frac{|\mathbf{e}'|}{|\mathbf{z}|}\right)^\ell \cdot \left(\frac{|\mathbf{e}|}{|\mathbf{z}|}\right)^\ell P_\ell(\hat{\mathbf{e}}\cdot\hat{\mathbf{e}}'). \tag{A14}$$

Suppose, to simplify, that the sphere is normalized to unity. We thus have

$$(\Delta\sigma, F^{m,e}) = a'^m \sum_{a',e'} \alpha_{a'}^{e'} \sum_\ell \ell^{2m} |e'|^\ell |e|^\ell P_\ell(\hat{\mathbf{e}}\cdot\hat{\mathbf{e}}'). \tag{A15}$$

We recognize here the weighting function introduced in section 3:

$$(\Delta\sigma, F^{m,e}) = a'^m \sum_{a',e'} \alpha_{a'}^{e'} a'^m \left(|\mathbf{e}|\partial_{|\mathbf{e}|}\right)^{2m} \left(\frac{1}{|\mathbf{e}'|} \frac{1}{\left|\mathbf{e} - \frac{\mathbf{e}'}{|\mathbf{e}'|}\right|}\right). \tag{A16}$$

[75] Finally, to compute the wavelet analysis of the gravity effect of a bathymetric load, one only has to multiply the coefficients of the discrete wavelet representation of the bathymetry with another set of functions.

[76] **Acknowledgments.** The authors thank Alain Bonneville for providing the ship data and the bathymetric grid and for many fruitful discussions. The GeoForschungs Zentrum Potsdam is also gratefully acknowledged for providing the CHAMP magnetic data. We would also like to thank Stefan Maus for his help with the CHAMP magnetic data preprocessing, Olivier De Viron for helping us to improve our manuscript, and Armand Galdeano and Mioara Mandea for fruitful discussions. Finally, we also thank Frederik J. Simons, Jean-Claude Mareschal, and an anonymous reviewer for their careful reviews that contributed to improve our manuscript. The gravity field study was also supported by CNES. Aude Chambodut was supported by a Lavoisier fellowship from the Ministère Français des Affaires Etrangères. All maps were plotted using the GMT software [*Wessel and Smith*, 1995]. This is IPGP contribution 2125.

References

Adam, C., and A. Bonneville (2005), Extent of the South Pacific Superswell, *J. Geophys. Res.*, *110*, B09408, doi:10.1029/2004JB003465.

Adam, C., V. Vidal, and A. Bonneville (2005), MiFil: A method to characterize seafloor swells with application to the south central Pacific, *Geochem. Geophys. Geosyst.*, *6*, Q01003, doi:10.1029/2004GC000814.

Andersen, O. B., and P. Knudsen (1998), Global marine gravity field from the ERS-1 and Geosat geodetic mission altimetry, *J. Geophys. Res.*, *103*, 8129–8137.

Anderson, D. (1995), Lithosphere, asthenosphere, and perisphere, *Rev. Geophys.*, *33*, 125–149.

Anderson, D. (1998), The scales of mantle convection, *Tectonophysics*, *284*, 1–17.

Baudry, N., and L. Kroenke (1991), Intermediate-wavelength (400–600 km), South Pacific geoidal undulations: Their relationship to linear volcanic chains, *Earth Planet. Sci. Lett.*, *102*, 430–443.

Binard, N., R. Hekinian, J. L. Cheminee, R. C. Searle, and P. Stoffers (1991), Morphological and structural studies of the Society and Austral hotspot regions in the South Pacific, *Tectonophysics*, *186*, 293–312.

Caress, D., M. McNutt, R. Detrick, and J. Mutter (1995), Seismic imaging of hotspot-related crustal underplating beneath the Marquesas Islands, *Nature*, *373*, 600–603.

Cazenave, A., S. Houry, B. Lago, and K. Dominh (1992), Geosat-derived geoid anomalies at medium wavelength, *J. Geophys. Res.*, *97*, 7081–7096.

Chambodut, A., I. Panet, M. Mandea, M. Diament, M. Holschneider, and O. Jamet (2005), Wavelet frames: An alternative to spherical harmonic representation of potential fields, *Geophys. J. Int.*, *163*(3), 875–899, doi:10.1111/j.1365-246X.2005.02754.x.

Cohen, Y., and J. Achache (1990), New global vector magnetic anomaly maps derived from Magsat data, *J. Geophys. Res.*, *95*, 10,783–10,800.

Cohen, Y., and J. Achache (1994), Contribution of induced and remanent magnetization to long-wavelength oceanic magnetic anomalies, *J. Geophys. Res.*, *99*, 2943–2954.

Courtillot, V., A. Davaille, J. Besse, and J. Stock (2003), Three distinct types of hotspots in the Earth's mantle, *Earth Planet. Sci. Lett.*, *205*, 295–308.

Davaille, A. (1999), Simultaneous generation of hotspots and superswells by convection in a heterogeneous planetary mantle, *Nature*, *402*, 756–760.

Diament, M., and N. Baudry (1987), Structural trends in the Southern Cook and Austral archipelagoes (South Central Pacific) based on an analysis of Seasat data: Geodynamic implications, *Earth Planet. Sci. Lett.*, *85*, 427–438.

Dyment, J., and J. Arkani-Hamed (1998), Contribution of lithospheric remanent magnetization to satellite magnetic anomalies over the world's oceans, *J. Geophys. Res.*, *103*, 15,423–15,441.

Dziewonski, A. M., and D. L. Anderson (1981), Preliminary Reference Earth Model (PREM), *Phys. Earth Planet. Inter.*, *25*, 297–356.

Ekström, G., and A. Dziewonski (1998), The unique anisotropy of the Pacific upper mantle, *Nature*, *394*, 168–172.

Fengler, M. J., W. Freeden, A. Kohlhaas, V. Michel, and T. Peters (2005), Wavelet modelling of regional and temporal variations of the Earth's gravitational potential observed by GRACE, *Schr. Funktionalanal. Geomathemat.*, *21*, 1–11.

Filmer, P. E., M. K. McNutt, H. F. Webb, and D. J. Dixon (1993), Volcanism and archipelagic aprons in the Marquesas and Hawaiian islands, *Mar. Geophys. Res.*, *16*, 385–406.

Fleitout, L., and C. Moriceau (1992), Short-wavelength geoid, bathymetry and convective pattern beneath the Pacific Ocean, *Geophys. J. Int.*, *110*, 6–28.

Forte, A., and R. Peltier (1991), Viscous flow models of global geophysical observables: 1. Forward problems, *J. Geophys. Res.*, *96*, 20,131–20,159.

Gu, Y. J., A. M. Dziewonski, W. Su, and G. Ekström (2001), Models of the mantle shear velocity and discontinuities in the pattern of lateral heterogeneities, *J. Geophys. Res.*, *106*, 11,169–11,199.

Hackney, R. I., and W. E. Featherstone (2003), Geodetic versus geophysical perspectives of the 'gravity anomaly', *Geophys. J. Int.*, *154*, 35–43.

Hager, B., R. Clayton, M. Richard, R. Comer, and A. Dziewonski (1985), Lower mantle heterogeneity, dynamic topography and the geoid, *Nature*, *313*, 541–545.

Haxby, W. F., and J. K. Weissel (1986), Evidence for small-scale convection from Seasat altimeter data, *J. Geophys. Res.*, *91*, 3507–3520.

Holschneider, M. (1995), *Wavelets: An Analysis Tool*, 423 pp., Clarendon, Oxford, U.K.

Holschneider, M., A. Chambodut, and M. Mandea (2003), From global to regional analysis of the magnetic field on the sphere using wavelet frames, *Phys. Earth Planet. Inter.*, *135*, 107–124.

Ito, G., M. McNutt, and R. Gibson (1995), Crustal structure of the Tuamotu plateau, 15°S, and implications for its origin, *J. Geophys. Res.*, *100*, 8097–8114.

Jackson, A., A. Jonkers, and M. Walker (2000), Four centuries of geomagnetic secular variation from historical records, *Philos. Trans. R. Soc. London*, *358*, 957–990.

Jekeli, C. (1981), Alternative methods to smooth the Earth's gravity field, *Rep. 327*, Dep. of Civ. and Environ. Eng. and Geod. Sci., Ohio State Univ., Columbus.

Johnson, C. L., and C. G. Constable (1998), Persistently anomalous Pacific geomagnetic fields, *Geophys. Res. Lett.*, *25*, 1011–1014.

Jordahl, K. A., M. K. McNutt, H. F. Webb, S. E. Kruse, and M. G. Kuykendall (1995), Why there are no earthquakes on the Marquesas Fracture Zone, *J. Geophys. Res.*, *100*, 24,431–24,447.

Kuvshinov, A., and N. Olsen (2005), 3D modelling of the magnetic field due to ocean tidal flow, in *Earth Observation With CHAMP: Results from Three Years in Orbit*, edited by C. Reigber et al., pp. 359–365, Springer, New York.

LaBrecque, J. L., and C. A. Raymond (1985), Seafloor spreading anomalies in the MAGSAT field of the North Atlantic, *J. Geophys. Res.*, *90*, 2565–2575.

Langel, R. A. (1987), The main geomagnetic field, in *Geomagnetism*, edited by J. A. Jacobs, chapter 4, Elsevier, New York.

Lesur, V. (2006), Introducing localized constraints in global geomagnetic field modelling, *Earth Planets Space*, *58*, 477–483.

Lowes, F. J. (1974), Spatial power spectrum of the main geomagnetic field and extrapolation to the core, *Geophys. J. R. Astron. Soc.*, *36*, 717–730.

Maia, M., and M. Diament (1991), An analysis of the altimetric geoid in various wavebands in the central Pacific Ocean: Constraints on the origin of intraplate features, *Tectonophysics*, *190*, 133–153.

Martelet, G., P. Sailhac, F. Moreau, and M. Diament (2001), Characterization of geological boundaries using 1D-wavelet transform on gravity data: Theory and application to the Himalaya, *Geophysics*, *66*(4), 1116–1129.

Maus, S., M. Rother, R. Holme, H. Lhr, N. Olsen, and V. Haak (2002), First scalar magnetic anomaly map from CHAMP satellite data indicates weak lithospheric field, *Geophys. Res. Lett.*, *29*(14), 1702, doi:10.1029/2001GL013685.

Maus, S., M. Rother, K. Hemant, C. Stolle, H. Lühr, A. Kuvshinov, and N. Olsen (2006), Earth's lithospheric magnetic field determined to spherical harmonic degree 90 from CHAMP satellite measurements, *Geophys. J. Int.*, *164*(2), 319–330, doi:10.1111/j.1365-246X.2005.02833.x.

McNutt, M. K. (1998), Superswells, *Rev. Geophys.*, *36*, 211–244.

McNutt, M., and A. Bonneville (2000), A shallow, chemical origin for the Marquesas Swell, *Geochem. Geophys. Geosyst.*, *1*(6), doi:10.1029/1999GC000028.

McNutt, M., and K. Fischer (1987), The South Pacific Superswell, in *Seamounts, Islands, and Atolls*, *Geophys. Monogr. Ser.*, vol. 43, edited by B. H. Keating et al., pp. 25–34, AGU, Washington, D. C.

McNutt, M. K., and A. Judge (1990), The superswell and mantle dynamics beneath the South Pacific, *Science*, *248*, 969–975.

Merrill, R. T., M. W. McElhinny, and P. L. McFadden (1998), *The Magnetic Field of the Earth*, *Int. Geophys. Ser.*, vol. 63, Elsevier, New York.

Moreau, F., D. Gibert, M. Holschneider, and G. Saracco (1999), Identification of sources of potential fields with the continuous wavelet transform: Basic theory, *J. Geophys. Res.*, *104*, 5003–5013.

Morgan, W. (1972), Plate motions and deep mantle convection, *Mem. Geol. Soc. Am.*, *132*, 5355–5360.

Moritz, H. (1989), *Advanced Physical Geodesy*, 2nd ed., Wichmann, Karlsruhe, Germany.

Müller, R. D., W. R. Roest, J. Y. Royer, L. M. Gahagan, and J. G. Sclater (1997), Digital isochrons of the world's oceans floor, *J. Geophys. Res.*, *102*, 3211–3214.

Niu, F., S. Solomon, P. Silver, D. Suetsugu, and H. Inoue (2002), Mantle transition-zone structure beneath the South Pacific Superswell and evidence for a mantle plume underlying the Society hot-spot, *Earth Planet. Sci. Lett.*, *198*, 371–380.

Okal, E., J. Talandier, K. Sverdrup, and T. Jordan (1980), Seismicity and tectonic stress in the South-Central Pacific, *J. Geophys. Res.*, *85*, 6479–6495.

Pavlis, N. K. (1988), Modeling and estimation of a low degree geopotential model from terrestrial gravity data, *Rep. 386*, Dep. of Geod. Sci. and Surv., Ohio State Univ., Columbus.

Purucker, M., and J. Dyment (2000), Satellite magnetic anomalies related to seafloor spreading in the South Atlantic Ocean, *Geophys. Res. Lett.*, *27*, 2765–2768.

Purucker, M., T. Sabaka, N. Olsen, and S. Maus (2003), How have Ørsted, CHAMP, and SAC-C improved our knowledge of the oceanic regions, in *OIST-4 Proceedings*, edited by P. Stauning et al., pp. 89–94, Dan. Meteorol. Inst., Copenhagen.

Richter, F. (1973), Convection and large-scale circulation of the mantle, *J. Geophys. Res.*, *78*, 8735–8745.

Robinson, E., and B. Parsons (1988), Effect of a shallow low-viscosity zone on small-scale instabilities under the cooling oceanic plates, *J. Geophys. Res.*, *93*, 3469–3479.

Romanowicz, B., and Y. Gung (2002), Superplumes from the core-mantle boundary to the lithosphere: Implications for heat flux, *Science*, *296*, 513–516.

Sabaka, T. J., N. Olsen, and M. E. Purucker (2004), Extending comprehensive models of the Earth's magnetic field with Ørsted and CHAMP, *Geophys. J. Int.*, *159*(2), 521–547.

Sailhac, P., and D. Gibert (2003), Identification of sources of potential fields with the continuous wavelet transform: Two-dimensional wavelets and multipolar approximations, *J. Geophys. Res.*, *108*(B5), 2262, doi:10.1029/2002JB002021.

Simons, F. J., F. A. Dahlen, and M. A. Wieczorek (2006), Spatiospectral concentration on a sphere, *SIAM Rev.*, in press.

Sleep, N. H. (1990), Hotspots and mantle plumes: Some phenomenology, *J. Geophys. Res.*, *95*, 6715–6736.

Smith, W., and D. Sandwell (1997), Global sea-floor topography from satellite altimetry and ship depth soundings, Data version 8.2, *Science*, *277*, 1956–1962.

Talandier, J., and E. Okal (1987), Crustal structure in the Society and Tuamotu islands, French Polynesia, *Geophys. J. R. Astron. Soc.*, *88*, 499–528.

Tapley, B. D., S. Bettadpur, M. Watkins, and C. Reigber (2004), The gravity recovery and climate experiment: Mission overview and early results, *Geophys. Res. Lett.*, *31*, L09607, doi:10.1029/2004GL019920.

Turner, D. L., and R. D. Jarrard (1982), K-Ar dating of the Cook-Austral island chain: A test of the hot-spot hypothesis, *J. Volcanol. Geotherm. Res.*, *12*, 187–220.

Tyler, R., S. Maus, and H. Lühr (2003), Satellite observations of magnetic fields due to ocean tidal flow, *Science*, *299*, 239–241.

Vening-Meinesz, F. A. (1941), Gravity over the Hawaiian archipelago and over the Madiera area: Conclusions about the Earth's crust, *Proc. K. Akad. Wetensia*, *44*, 1–12.

Wahr, J., M. Molenaar, and F. Bryan (1998), Time variability of the Earth's gravity field: Hydrological and oceanic effects and their possible detection using GRACE, *J. Geophys. Res.*, *103*, 30,205–30,229.

Walcott, R. I. (1970), Flexure of the lithosphere at Hawaii, *Tectonophysics*, *9*, 435–446.

Walker, A. D., and G. E. Backus (1996), On the difference between the average values of Br2 in the Atlantic and Pacific hemispheres, *Geophys. Res. Lett.*, *23*, 1965–1968.

Watts, A. B. (1978), An analysis of isostasy in the world's oceans: 1. Hawaiian-Emperor Seamount chain, *J. Geophys. Res.*, *83*, 5889–6004.

Wessel, P., and W. H. F. Smith (1995), New version of the Generic Mapping Tools released, *Eos Trans. AGU*, *76*, 329.

Wessel, P., D. Bercovici, and L. Kroenke (1994), The possible reflection of mantle discontinuities in Pacific geoid and bathymetry, *Geophys. Res. Lett.*, *21*, 18, 1943–1946.

Wieczorek, M., and F. J. Simons (2005), Localized spectral analysis on the sphere, *Geophys. J. Int.*, *162*(3), 655–675, doi:101111/j.1365-246X.2005.02687.x.

Yuen, D., and L. Fleitout (1984), Stability of the oceanic lithosphere with variable viscosity: An initial value approach, *Phys. Earth Planet. Inter.*, *34*, 173–185.

A. Chambodut, Department of Applied and Industrial Mathematics, University of Potsdam, Am Neuen Palais 10, D-14469, Potsdam, Germany. (chambodu@math.uni-potsdam.de)

M. Diament and I. Panet, Institut de Physique du Globe de Paris, Case 89, 4, place Jussieu, F-75252 Paris Cedex 05, France. (diament@ipgp.jussieu.fr; panet@ipgp.jussieu.fr)

M. Holschneider, Department of Mathematics, University of Potsdam, Am Neuen Palais 10, D-14469, Potsdam, Germany. (hols@math.uni-potsdam.de)

O. Jamet, Laboratoire de Recherche en Géodésie, Institut Géographique National, 6/8 avenue Blaise Pascal, Cité Descartes, Champs-sur-Marne, F-77455 Marne-la-Vallée Cedex 2, France. (jamet@ensg.ign.fr)